The impact of recent and future calving events on the Larsen C ice shelf

Tom Mitcham[1], G. Hilmar Gudmundsson[2], and Jonathan L. Bamber[1]

[1]Bristol Glaciology Centre, School of Geographical Sciences, University of Bristol, Bristol, UK
[2]Department of Geography and Environmental Sciences, Northumbria University, Newcastle, UK

Correspondence: Tom Mitcham (tom.mitcham@bristol.ac.uk)

Abstract. The Antarctic Peninsula has seen rapid and widespread changes in the extent of its ice shelves in recent decades, including the collapse of the Larsen A and B ice shelves in 1995 and 2002, respectively. In 2017 the Larsen C ice shelf (LCIS) lost around 10% of its area by calving one of the largest icebergs ever recorded (A68). This has raised questions about the structural integrity of the shelf and the impact of any changes in its extent on the flow of its tributary glaciers. In this work, we

5   used an ice flow model to study the instantaneous impact of changes in the thickness and extent of the LCIS on ice dynamics, and in particular on changes in the grounding line flux (GLF). We initialised the model to a pre-A68 calving state, and first replicated the calving of the A68 iceberg. We found that there was a limited impact on upstream flow – with speeds increasing by less than 10% across almost all of the shelf – and a 0.5% increase in GLF. This result is supported by observations of ice velocity made before and after the calving event. We then perturbed the ice-shelf geometry through idealised calving and

10 thinning experiments of increasing magnitude. We found that significant changes to the geometry of the ice shelf, through both calving and thinning, resulted in limited changes in GLF. For example, to produce a doubling of GLF from calving, the new calving front needed to be moved to 5 km from the grounding line, removing almost the entire ice shelf. For thinning, over 200 m of the ice-shelf thickness had to be removed across the whole shelf to produce a doubling of GLF. Calculating the increase in GLF (607%) after removing the entire ice shelf allowed us to quantify the total amount of buttressing provided by

15 the LCIS. From this, we identified that the region of the ice shelf in the first 5 km downstream of the grounding line provided over 80% of the buttressing capacity of the shelf. This is due to the large resistive stresses generated in the narrow, local embayments downstream of the largest tributary glaciers.

1   Introduction

Around 74% of the Antarctic coastline is fringed by floating ice shelves (Bindschadler et al., 2011). These ice shelves are fed

20 by tributary glaciers and ice streams, and lose mass predominantly through basal melting at the ice-ocean interface, and calving at the ice front (Depoorter et al., 2013). When formed in embayments, or where they locally run aground at ice rises or pinning points, ice shelves can generate resistive stresses which are transferred through the ice shelf to the grounding line (GL), where they provide a backstress to the grounded ice sheet (Thomas, 1979). This process, known as ice-shelf buttressing, means that

ice shelves can exert a mechanical control on the grounding line flux (GLF), and therefore control the rate at which the ice

25   sheet contributes to changes in global sea level (e.g. Dupont and Alley, 2005; Gudmundsson, 2013).

The Larsen C ice shelf (LCIS) is situated on the eastern side of the northern Antarctic Peninsula (AP), and is the fourth largest ice shelf in Antarctica. Over the second half of the 20th century, increasing surface air temperatures – and a subsequent increase in surface melt – have been implicated in the breakup of several ice shelves on the AP (e.g. Morris and Vaughan, 2003; Vaughan et al., 2003; Khazendar et al., 2011; Banwell et al., 2013). In 1995 the Larsen A ice shelf (LAIS) collapsed (Rott et al.,

30   1996), and in 2002, the Larsen B ice shelf (LBIS) disintegrated in a matter of six weeks (Scambos et al., 2004). Domack et al. (2005) showed from a subsequent analysis of marine sediments that the LBIS had been present for at least 12,000 years.

In 2017, the LCIS calved one of the largest icebergs ever recorded – named A68 – reducing its surface area by $\sim 10\%$. The ice-shelf extent is now at its minimum since satellite observations began (Hogg and Gudmundsson, 2017). During the 2019/20 austral summer, the LCIS experienced near-record levels of surface melting (Bevan et al., 2020). All of these factors have

35   raised questions about the future viability of the LCIS (e.g. Kulessa et al., 2014; Jansen et al., 2015; Holland et al., 2015), and what the consequences of any changes to its thickness or extent might be for the ice dynamics of the AP.

Following the collapse of the LBIS in 2002, a significant change in the flow of its tributary glaciers was observed, with some increasing in speed by close to 900% (Rignot et al., 2004). This increase in ice speeds – and consequently GLF – has been sustained to the present day (Berthier et al., 2012; Rott et al., 2018). De Rydt et al. (2015) modelled the response to this

40   rapid loss of ice-shelf buttressing through diagnostic (or time-independent) simulations with the ice flow model Úa, which is also used in this study. They were able to reproduce the spatial variability of the response in ice velocity across the tributary glaciers, but suggested that transient experiments would be required to simulate the observed, quantitative changes. A similar approach – also using Úa – was taken to model the response to the collapse of the LAIS (Royston and Gudmundsson, 2016). This study found that the initial increase in GLF could be reproduced with diagnostic experiments, but that modelling the

45   transient redistribution of mass was required to reproduce changes further upstream in the tributary glaciers.

A number of studies have previously examined buttressing on the LCIS. Borstad et al. (2013) modelled the stress field in the ice shelf, calculated a local buttressing number, and modelled the impact of removing basal contact at ice rises on the dynamics of the shelf, but not the tributary glaciers. Fürst et al. (2016) mapped the 'maximum buttressing' number across the ice shelf, and from this delineated regions of 'passive ice' which could be calved without significantly increasing the ice flux across

50   new calving fronts in the shelf. Reese et al. (2018) computed the impact of small perturbations in ice-shelf thickness on the integrated GLF, producing a map of the 'buttressing flux response number' across the shelf. This allowed them to determine the regions in the ice shelf where a perturbation in ice thickness would produce the largest response in GLF, and they also demonstrated that small changes in ice-shelf thickness could impact the GLF hundreds of kilometres away. Finally, Zhang et al. (2020) explored the correlation between locally derived buttressing numbers in the ice shelf, and changes in GLF due to

55   small perturbations in ice-shelf thickness at the same locations. They found that for a real-world ice shelf (the LCIS) there was no relationship between these two measures, and that locally derived buttressing numbers are not predictors for the impact of perturbations in ice-shelf geometry on GLF.

Here, we build on this existing literature on the ice dynamics of the LCIS through a series of diagnostic perturbation experiments of increasing magnitude. Our first objective was to model the response of the LCIS and its tributaries to the calving of the A68 iceberg and validate these results with observations. We then studied the GLF response to a series of idealised ice-shelf calving events. From quantifying the maximum GLF response, we determined the total amount of buttressing provided by the ice shelf, and examined what proportion of this total is generated by different regions of the shelf. We simulate the loss of contact of the ice shelf from the Bawden and Gipps ice rises, again examining the impact on GLF. And finally, we systematically perturb the thickness of the ice shelf by increasing amounts, again aiming to understand how much the ice-shelf geometry needs to change before a significant response in GLF is produced.

2   Methods

2.1   Ice flow model

We used the Úa ice flow model (Gudmundsson et al., 2012), which solves the vertically integrated, shallow-shelf approximation (e.g. MacAyeal, 1989) using the finite element method on an unstructured mesh. Úa has been used in both idealised (e.g. Gudmundsson et al., 2012; Gudmundsson, 2013) and realistic (e.g. De Rydt et al., 2015; Minchew et al., 2017; Hill et al., 2018; Reese et al., 2018; Gudmundsson et al., 2019) settings to examine the response of grounded ice to perturbations in the ice shelf. It has also been tested in recent model intercomparison projects (Pattyn et al., 2013; Cornford et al., 2020).

The equation solved in Úa for the vertically integrated balance of stresses is

$$\boldsymbol{\nabla}_{xy} \cdot (h\boldsymbol{R}) - \boldsymbol{t_{bh}} = \rho_i gh \boldsymbol{\nabla}_{xy} s + \frac{1}{2} gh^2 \boldsymbol{\nabla}_{xy} \rho_i, \tag{1}$$

where

$$\boldsymbol{R} = \begin{pmatrix} 2\tau_{xx} + \tau_{yy} & \tau_{xy} \\ \tau_{xy} & 2\tau_{yy} + \tau_{xx} \end{pmatrix} \tag{2}$$

is the resistive stress tensor, τ_{ij} are the components of the deviatoric stress tensor, $\boldsymbol{\nabla}_{xy} = (\partial_x, \partial_y)^T$, $\boldsymbol{t_{bh}}$ is the horizontal component of the basal traction, h is the ice thickness, s is the ice surface elevation, ρ_i is the vertically integrated ice density (which varies spatially) and g is the acceleration due to gravity.

In this work, we solved the equations for stress balance in a diagnostic, or time-independent mode, together with Glen's flow law, the constitutive equation linking the stress field in the ice to deformation

$$\dot{\epsilon}_{ij} = A\tau^{(n-1)}\tau_{ij} \tag{3}$$

where $\dot{\epsilon}_{ij}$ are the components of the strain rate tensor, τ is the second invariant of the deviatoric stress tensor, given by

$$\tau = \sqrt{\tau_{ij}\tau_{ij}/2} \tag{4}$$

and the rate factor, A – which depends on ice properties including temperature, crystal fabric and damage – was optimised using inverse methods (see Sect. 2.3). We chose the creep exponent $n = 3$.

A non-linear, Weertman type sliding law was used with the following form

$$\boldsymbol{t_{bh}} = C^{-1/m}||\boldsymbol{u_b}||^{(1-m)/m}\boldsymbol{u_b} \tag{5}$$

where $\boldsymbol{t_{bh}}$ is the horizontal component of the the bed-tangential basal traction and $\boldsymbol{u_b}$ the horizontal component of the bed-
tangential ice velocity. The basal slipperiness parameter, C, is also inferred using inverse methods, and $m = 3$. The results of
diagnostic perturbation experiments using this ice flow model have previously been found to be largely unaffected by the value
chosen for m (e.g. Hill et al., 2018; Gudmundsson et al., 2019).

2.2 Model domain and data

The model domain, shown in Fig. 1, includes all of the drainage basins identified by Cook and Vaughan (2010) that drain
into the LCIS. The calving front location represents a pre-July 2017 state, before the A68 iceberg calved from the shelf. One
artificial boundary was drawn to separate the region between the Larsen C and D ice shelves, and this was manually delineated
by joining the ice divide to the calving front.

The finite element mesh used in the computation was generated with the open source Gmsh software (Geuzaine and Remacle,
2009), and used linear elements. The target element size was set to $2\,\mathrm{km}$ across the floating ice shelf, with the resolution
increased around the grounding line, where elements $250\,\mathrm{m}$ in size were used. The mesh was refined to $1\,\mathrm{km}$ in all tributary
glaciers, and $500\,\mathrm{m}$ in regions of high strain rates. This ultimately produced a mesh with $\sim 154{,}000$ elements with a maximum,
median, and minimum element size of $4{,}000\,\mathrm{m}$, $640\,\mathrm{m}$, and $160\,\mathrm{m}$ respectively. The dependence of the model results on element
size was tested in a convergence analysis, the results of which are shown in Appendix C.

Along the ice divides at the boundary of the model domain, a zero velocity boundary condition was applied. At the calving
front, a stress boundary condition, arising from ocean pressure, was prescribed.

The initial ice thickness, surface elevation and bedrock topography was taken from the Bedmachine Antarctica v2 data set
(Morlighem et al., 2019). The surface elevation was adjusted at a few points to ensure that at least $1\,\mathrm{m}$ of ice was present across
the whole computational domain. The firn air content field provided in this data set is derived from a firn densification model
(Ligtenberg et al., 2011), which was forced by RACMO2.3p2 at the surface (van Wessem et al., 2018). This field was used
to calculate a spatially variable, depth-integrated ice density across the model domain. Due to discrepancies between the ice
thickness and firn air content fields, it was necessary to introduce a minimum ice density of $800\,\mathrm{kgm^{-3}}$.

For the optimisation procedure used to initialise the model (see Sect. 2.3) we used the MEaSUREs InSAR-based Antarctic
Ice Velocity v2 data set (Rignot et al., 2011; Mouginot et al., 2012). For model validation (see Sect. 3.1) we used ice velocity
measurements generated from Sentinel-1 SAR data which were provided by ENVEO. This data set consisted of monthly maps
of tide-corrected ice velocities over the LCIS and its tributaries from October 2014 - September 2019.

2.3 Model initialisation

To generate initial conditions the rate factor, A and basal slipperiness parameter, C, were optimised by minimising the misfit
between observed and modelled ice velocity through inverse methods widely used in glaciology (e.g. MacAyeal, 1993). The
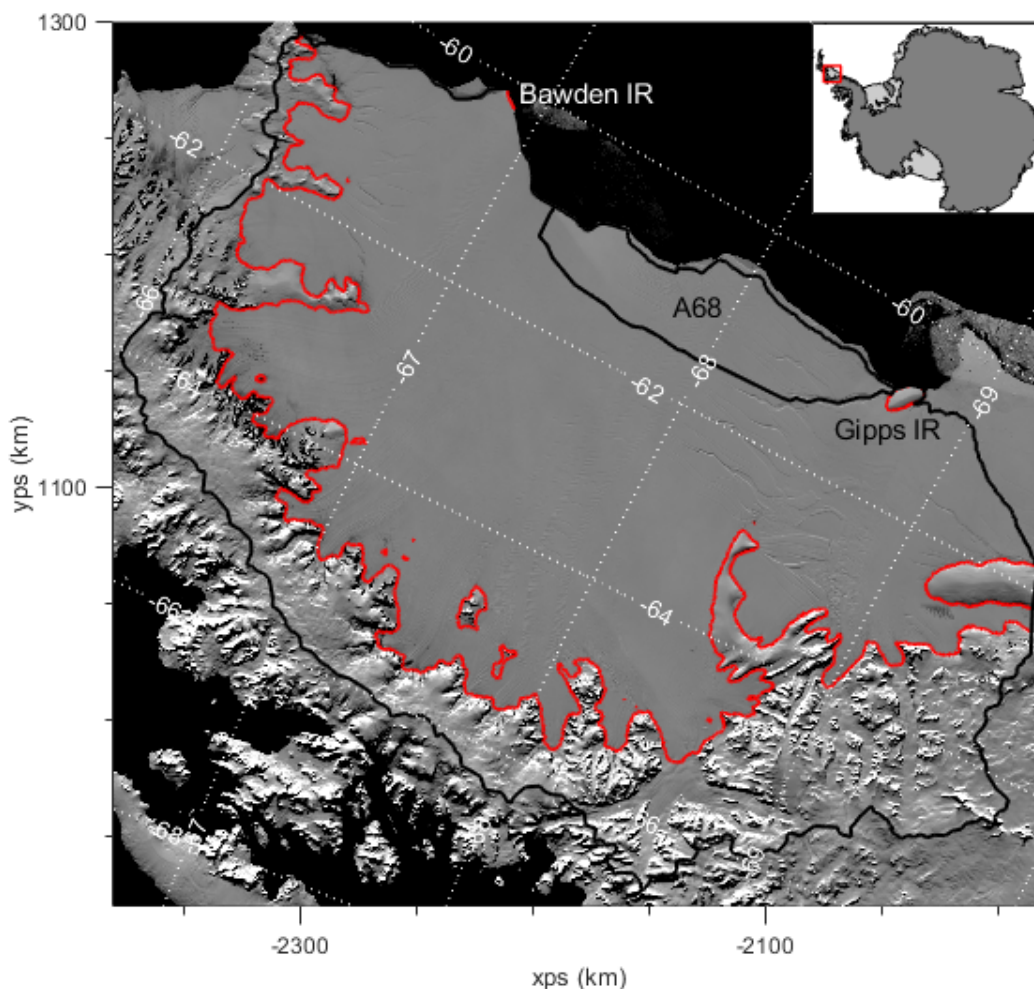
Figure 1. MODIS Mosaic of Antarctica (Scambos et al., 2007) image of the Larsen C ice shelf and its tributary glaciers, with open ocean shown in black. The boundary of the model domain is plotted in black, with the outline of the A68 iceberg which calved in July 2017 also shown. In red is the grounding line position as calculated in the model, which remains fixed throughout the experiments. The outlines of the Bawden and Gipps ice rises at the calving front of the ice shelf are also plotted in red. Lines of latitude and longitude are shown in the white, dotted lines. The coordinate system used here – and in all other maps – is the WGS84 Antarctic Polar Stereographic projection (EPSG:3031).

cost function that is minimised in Úa during the optimisation is $J = I + R$, where

120
$$I = \frac{1}{2\mathcal{A}} \int \left(\frac{\boldsymbol{u} - \boldsymbol{u_{obs}}}{\boldsymbol{u_{err}}} \right)^2 d\mathcal{A}, \tag{6}$$

is the misfit term, and

$$R = \frac{1}{2\mathcal{A}} \int \left[\gamma_s^2 \left(\left(\nabla \left(\log_{10}(A) - \log_{10}(\hat{A}) \right) \right)^2 + \left(\nabla \left(\log_{10}(C) - \log_{10}(\hat{C}) \right) \right)^2 \right) + \right.$$
$$\left. \gamma_a^2 \left(\left(\log_{10}(A) - \log_{10}(\hat{A}) \right)^2 + \left(\log_{10}(C) - \log_{10}(\hat{C}) \right)^2 \right) \right] d\mathcal{A}, \qquad (7)$$

is the regularisation term. Here, $\mathcal{A}$ is the area of the model domain, $\boldsymbol{u}$ is the modelled ice velocity and $\boldsymbol{u}_{obs}$ and $\boldsymbol{u}_{err}$ are the measured surface velocity and its associated uncertainty, both here taken from the MEaSUREs InSAR-based Antarctic Ice Velocity v2 data set. γ_s and γ_a are regularisation parameters that penalise deviation in the fields being optimised – in this case $\log_{10}(A)$ and $\log_{10}(C)$ – from their prior estimates – $\log_{10}(\hat{A})$ and $\log_{10}(\hat{C})$ – in terms of gradient and amplitude respectively. We used $\gamma_s = 1000$ and $\gamma_a = 1$, both determined from an L-curve analysis (see Appendix A).

The resulting ice velocity field is shown in Fig. 2b. There was a good fit to the observed velocities across the domain, with a spatially averaged RMS difference between the observed and modelled velocities of $11.2 \, \mathrm{ma}^{-1}$, and a particularly good fit across the ice shelf and at the GL. One region in which the model struggled to replicate the ice velocities is just to the north of the Gipps ice rise, where the nascent A68 iceberg was beginning to detach from the shelf. This gave rise to large strain rates in the shelf, which weren't captured in the model, presumably due to the regularisation applied to the rate factor, A. The resulting maps of A and C are shown in Fig. A2. Following the inversion, the modelled GLF across the main GL (i.e. excluding fluxes across ice rises in the shelf) was $23.2 \, \mathrm{Gta}^{-1}$, and this was the reference GLF to which GLF changes in perturbation experiments were compared.

2.4 Calving experiments

From the initial conditions derived from the initialisation procedure, the geometry of the ice shelf was perturbed whilst holding all other parameters constant, generating a new stress field. This yielded an instantaneous change in the modelled ice velocity, which we compared to the initial velocity field and from which we calculated changes in GLF.

The first experiment undertaken was to replicate the calving of the A68 iceberg, the extent of which was derived from Landsat 8 images. To perform the experiment, the mesh elements within the region that calved were removed, thereby relocating the model boundary to the new calving front. Through this procedure, the remaining elements of the mesh were left unchanged and any interpolation errors avoided.

In addition to the A68 calving event, a series of idealised calving experiments were conducted. The calving front was moved progressively nearer to the GL by removing mesh elements using a 'distance from the main grounding line' metric (mapped in Fig. 4c).

It is important to note that in these calving experiments (and indeed in all experiments in this study) no perturbation was applied to the nodal values of any element which crossed the main GL. This meant that there was no change in driving stresses across the GL, and that the GL location remained fixed in all experiments. This ensured that any change in GLF was due solely to changes in the buttressing provided by the ice shelf.
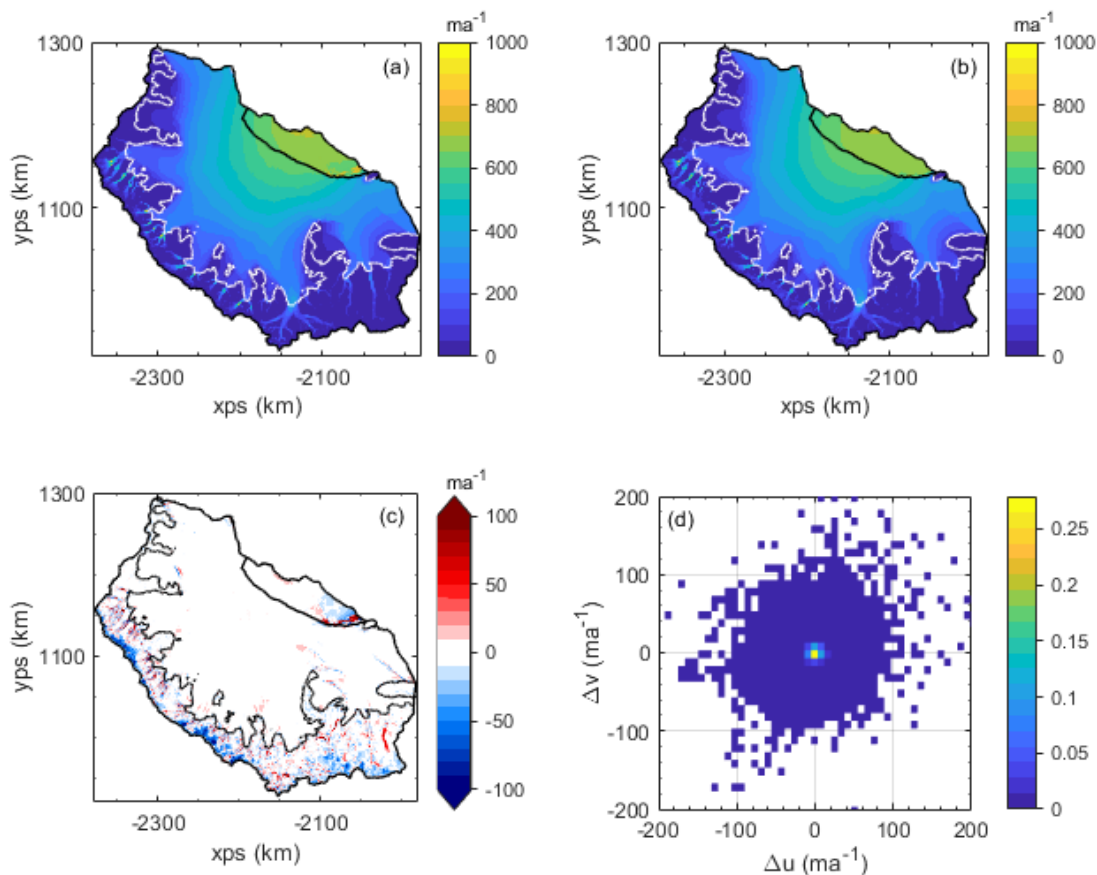
Figure 2. Observed ice speed **(a)** (from the MEaSUREs InSAR-based Antarctic ice velocity map) and modelled ice speed **(b)** following the initialisation procedure. Panel **(c)** shows the difference between the observed and modelled ice speed (obs - mod) and **(d)** is a normalised, bivariate histogram of the differences between the x and y components of the observed and modelled ice velocities at each node in the computational mesh.

2.5 Ungrounding and thinning experiments

To simulate the ungrounding of the LCIS from the Bawden and Gipps ice rises, the bed topography was lowered so that the ice shelf became afloat without changing the ice thickness. This experiment was carried out for the ungrounding from the two ice rises individually, and then for a 'combined' ungrounding, in which both contacts were removed simultaneously.

155   Finally, we explored the GLF response to perturbations in ice thickness. The ice thickness at nodes belonging to elements that were fully afloat (again, to ensure no change in driving stress across the GL) was progressively reduced until the whole ice shelf had a thickness of only 1 m. The 1 m thin layer of ice across the shelf was maintained for computational reasons, and the results are insensitive to a further reduction in the minimum ice thickness. Locally this thinning was done both proportionally,

i.e. the ice thickness was reduced by a given fraction of the total thickness at each node, and uniformly where thickness was

160   reduced across the whole ice shelf by the same fixed amount. The subsequent changes in ice velocity and GLF were calculated

for each step in the series of experiments.

3   Results

3.1   A68 calving

In response to the removal of the A68 iceberg from the model domain, there was an increase in ice velocity immediately

165   upstream of the new calving front of up to $\sim 100\,\mathrm{ma}^{-1}$ (Fig. 3a). The spatial extent of this velocity response was limited, and

across almost all of the ice shelf the change in velocity was smaller than 10% – even becoming negative in the region of the

shelf to the north of the Gipps ice rise. The changes in velocity did not extend throughout the whole ice shelf, and as such there

was almost no modelled increase in GLF (0.5%) due to this calving event.

We compared our model results to ice velocity observations produced and provided by ENVEO from analysis of Sentinel-1

170   SAR data. From this monthly time series of ice velocity maps, we calculated the mean and standard deviation in ice velocity

at each point in the model domain for both the October 2014 - June 2017 (pre-A68) and August 2017 - September 2019

(post-A68) periods (Fig. 3).

By plotting the 'signal' (the modelled response to A68 calving) to 'noise' (2σ variation in observations) ratio in Fig. 3b, and

examining the data along two flowlines on the shelf (Fig. 3 c and d), we see that the modelled response largely falls within the

175   internal variability of the ice velocity in the shelf. We also see that the mean ice velocity before and after the A68 calving event

are nearly identical, demonstrating that there was no observable, transient response to the calving of the A68.

3.2   Idealised calving experiments

The impact of moving the calving front progressively closer to the GL on the GLF can be seen in Fig. 4a and b. It shows that a

retreat of the calving front from its present day position back into the embayment produced a limited instantaneous impact on

180   the GLF. The calving front had to be retreated to $40\,\mathrm{km}$ from the GL to induce a 10% increase in GLF. For a doubling of GLF,

the calving front had to be positioned $5\,\mathrm{km}$ from the grounding line, removing almost all of the ice shelf in the process.

The maximum GLF increase (607%) – from the complete removal of the ice shelf – can be thought of as representing the

total buttressing provided by the LCIS to its grounded tributary glaciers. By comparing the GLF increase for each idealised

calving experiment to the maximum GLF increase from complete ice-shelf removal, we are able to calculate the proportion of

185   the total buttressing that remains after each perturbation experiment. Therefore, Fig. 4a and b show what proportion of the total

buttressing is provided by each section of the ice shelf removed in the series of calving perturbations. From this, we see that

over 95% of the total buttressing is provided by ice in the first $25\,\mathrm{km}$ downstream of the GL, and that over 80% is generated in

the first $5\,\mathrm{km}$ of ice immediately downstream of the GL.
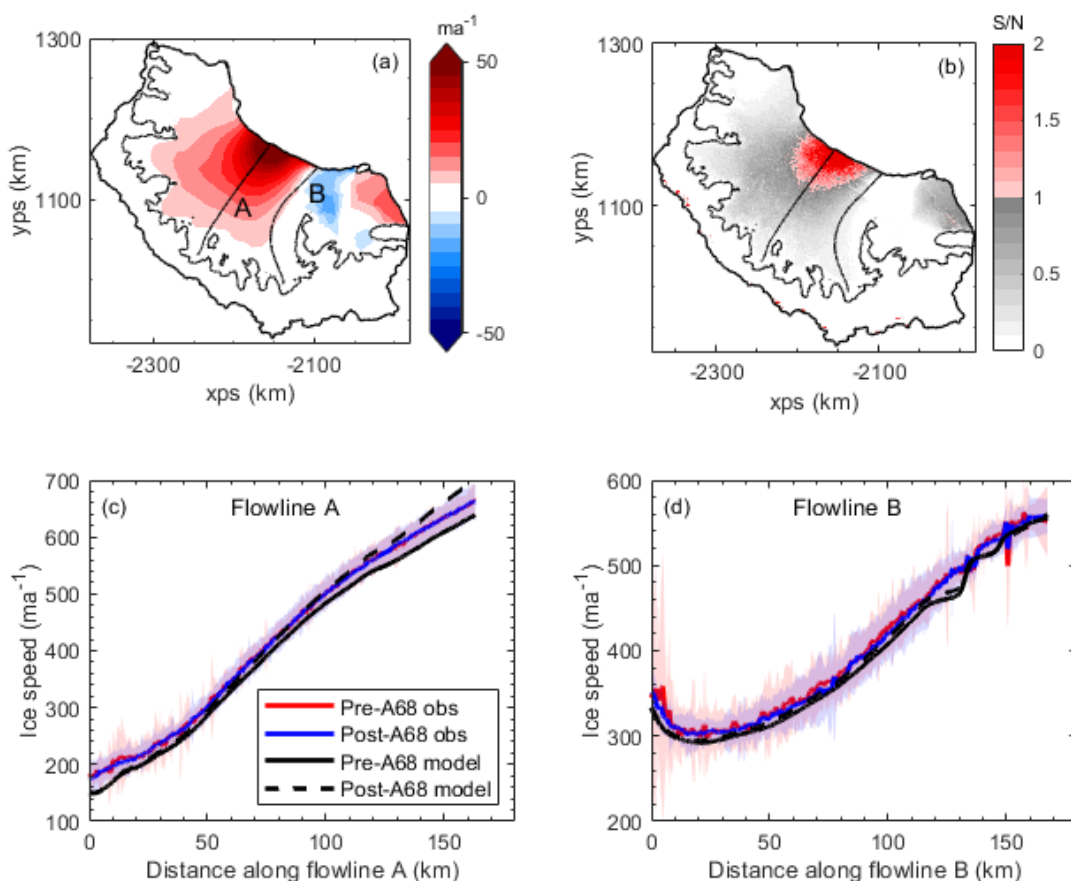
Figure 3. The modelled change in ice speed due to the calving of the A68 iceberg **(a)** along with the paths of the two flowlines used. **(b)** is the ratio of the 'signal' (model response in panel (a)) to the 'noise' (2σ variability in the monthly observations of ice velocity). Panels **(c)** and **(d)** show the modelled ice speed before and after the calving event along two flowlines in the shelf. The mean, observed speed before and after July 2017, together with shading representing the 2σ variability, is also plotted.

3.3 Ungrounding experiments

In the modelled response to the ungrounding of the LCIS from the Bawden ice rise there was a significant local increase in velocity upstream of the ice rise (Fig. 5a) of $\sim 200\ \mathrm{ma^{-1}}$ (and an even greater increase for the ice that was previously grounded). This represents a $\sim 50\%$ increase in ice velocity in this region. However, as with the A68 calving, this instantaneous velocity response is spatially limited and there is a just a 1% increase in GLF from this perturbation.

A similar, localised response in ice velocity is seen when the Gipps ice rise contact is removed (Fig. 5b), and a similar increase in GLF (1.2%) is modelled. Fig. 5c shows the ice velocity response to the simultaneous loss of contact from both ice rises, which produced an increase in velocity across the whole ice shelf. In Fig. 5d we show the difference between the com-
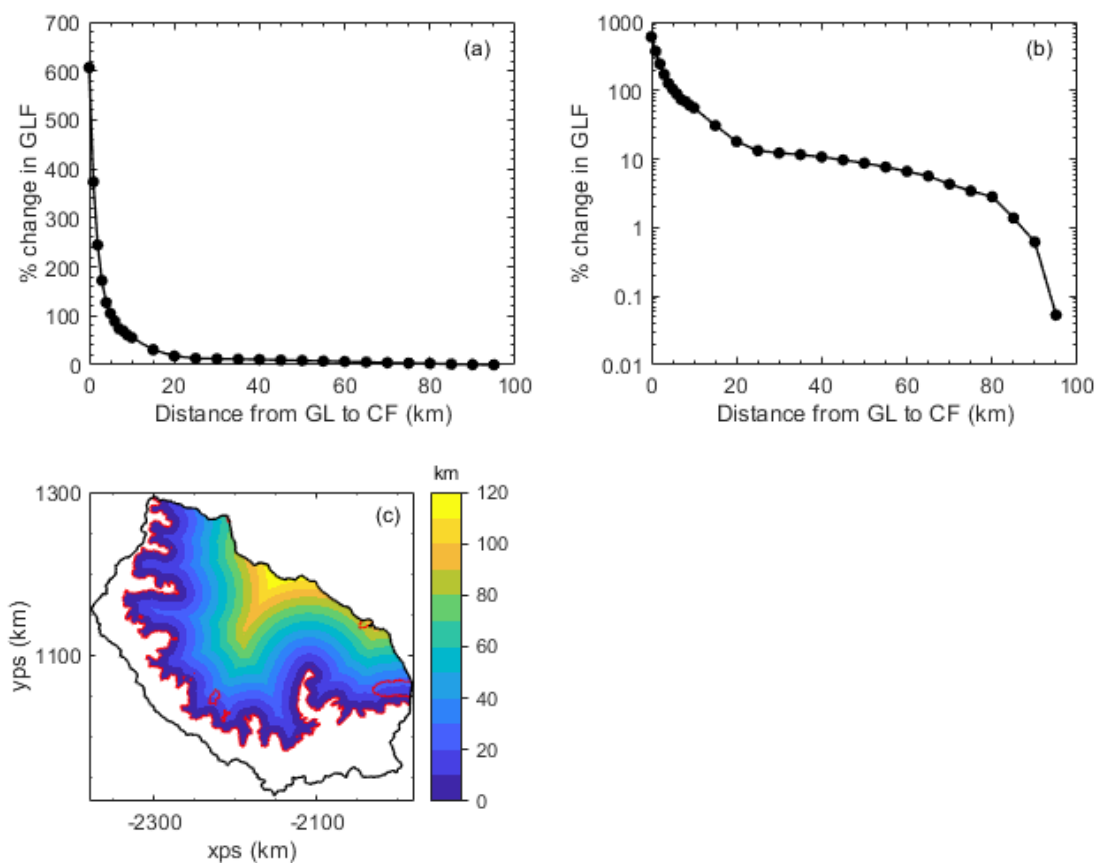
Figure 4. Calving experiments: **(a)** is the percentage change in grounding line flux for the each idealised calving experiment, and **(b)** shows the same data, but with a log scale on the y-axis. A map of the 'distance to the main grounding line' metric, used to define the calving experiments, is shown in **(c)**.

bined ungrounding event and the sum of the two individual events. It shows that the combined ungrounding is approximately a linear superposition of the two individual events, and the corresponding change in GLF from the combined event is 2.2%.

3.4 Thinning experiments

200 The changes in GLF due to perturbations in the ice-shelf thickness are shown in Fig. 6. When thinning the ice shelf in the 'uniform' sense (Fig. 6a) we find that ~ 30 m of ice-shelf thinning is required to produce a 10% increase in GLF and that over 200 m of thinning is required to produce a doubling of GLF.

The initial ice thickness across the model domain is shown in Fig. 6d. The maximum ice thickness in the shelf was 1,400 m, so a thinning perturbation larger than this had to be applied to reduce the ice shelf to the minimum thickness of 1 m everywhere.
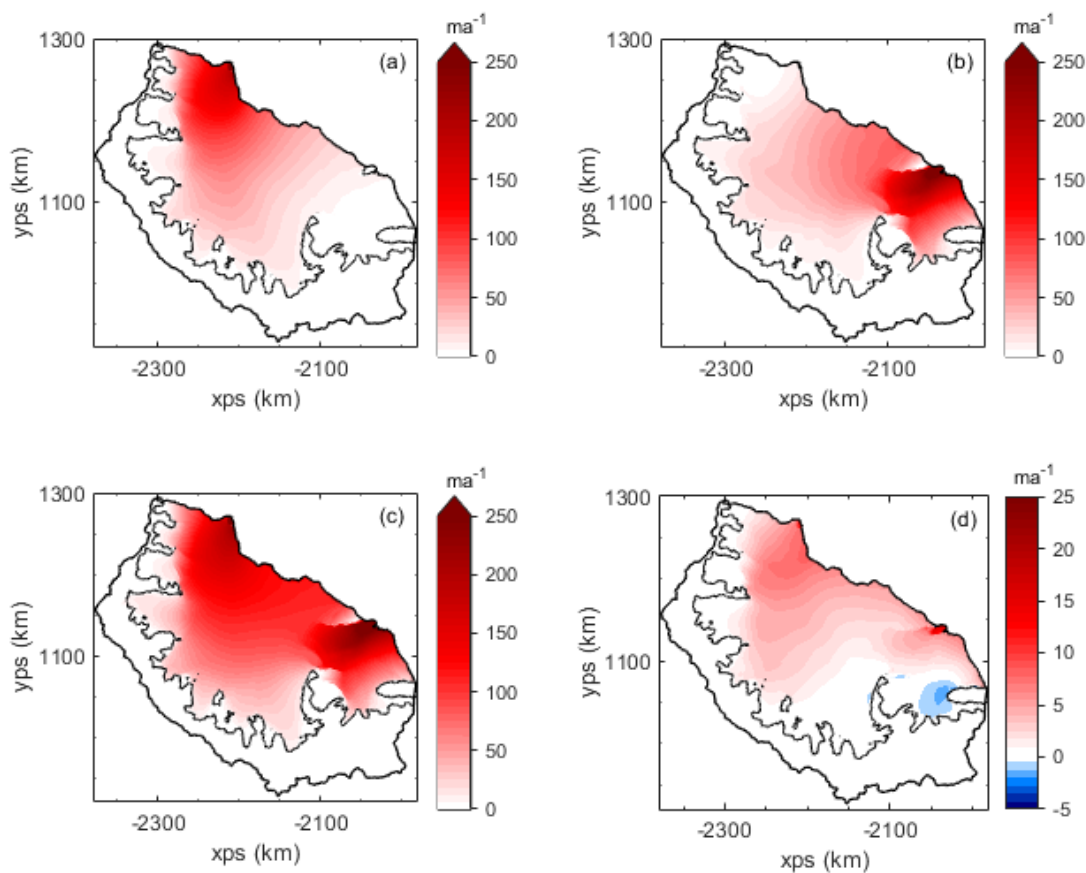
Figure 5. Ungrounding experiments: The change in modelled ice speed after ungrounding at the Bawden ice rise **(a)**, the Gipps ice rise **(b)** and at both ice rises simultaneously **(c)**. The difference between the combined ungrounding and the sum of the two individual ungrounding experiments is shown in **(d)**. Note the different scale on the colour bar in **(d)**, compared to those for panels **(a)**-**(c)**.

205 However, the median ice-shelf thickness was 290 m, 89% of the ice shelf had a thickness of less than 500 m and 99% less than 800 m. Therefore, the gradient of the curve in Fig. 6a decreases after $\sim$ 500 m of applied thinning as areas of the shelf already at the minimum thickness are not affected by further increases in perturbation amplitude.

 Fig. 6b shows the response in GLF to the 'proportional' thinning experiments. Here, 7% of the ice-shelf thickness needed to be removed to produce a 10% increase in GLF, and 45% removed to produce a doubling of GLF.

210 By calculating the ice-shelf mass removed in each experiment we were able to compare the two approaches (Fig. 6c). We see from the 'uniform' experiment curve, that there is a large response in GLF to a small change in mass removed towards the end of the series of perturbations, when the thickest ice is being significantly perturbed. The maximum GLF increase of 502%
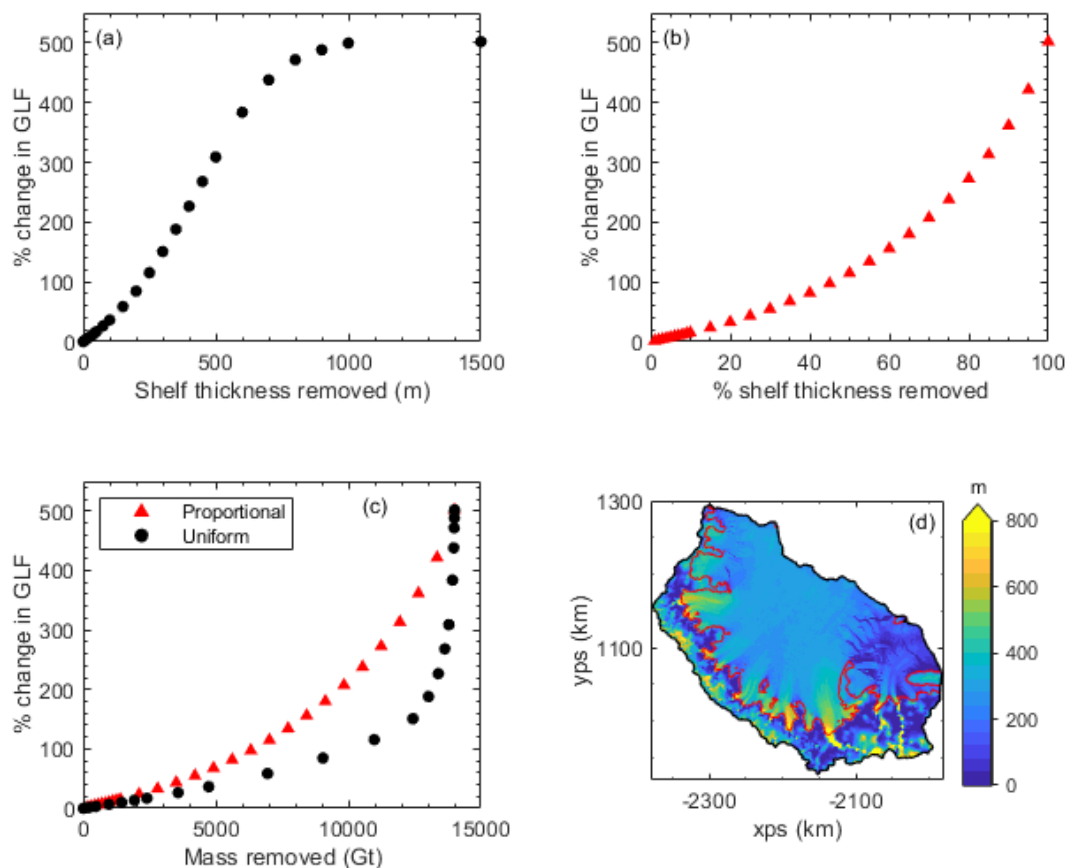
Figure 6. (a) is the percentage change in grounding line flux during the 'uniform' thinning experiments, and **(b)** is the same but for the 'proportional' thinning experiments. **(c)** is the response in grounding line flux for the two sets of experiments, but with the perturbations expressed in the amount of mass removed rather than the amount of thinning applied. **(d)** shows a map of ice thickness across the model domain from Bedmachine Antarctica v2 (Morlighem et al., 2019), with grounding lines plotted in red.

is identical in both the 'uniform' 1,500 m thinning and the 'proportional' 100% thinning experiments, as expected. The initial linear regimes in both sets of thinning perturbations are discussed in Appendix B.

4 Discussion

4.1 Calving experiments and ice-shelf buttressing

Our first objective was to model the response of the LCIS to the calving of the A68 iceberg and compare the results to observations. The limited change in ice-shelf velocities, and lack of change in the GLF, suggests that this part of the ice shelf

provided almost no buttressing. This finding is in agreement with the work of Fürst et al. (2016), who classified this region as

220   'passive ice', and with the map of 'buttressing flux response number' that Reese et al. (2018) produced. Borstad et al. (2017) hypothesised four potential calving events based on the trajectory in which the rift that eventually formed the A68 iceberg was growing, and modelled the response to these events. Their 'Scenario 2' is most similar to the calving event that eventually occurred, and our modelled results are in close agreement with theirs in both spatial pattern and amplitude (see Fig. 2d in Borstad et al., 2017).

225   The model results shows a decrease in ice velocity following the calving event in the region of the shelf just to the north of the Gipps ice rise. This is likely to be an artefact of the method used to perform the experiment. The rift that eventually formed the A68 iceberg had been present in the ice shelf for over a decade, and grew significantly during 2014 and 2016 (Jansen et al., 2015; Borstad et al., 2017). Therefore, the dynamic response to the detaching of the nascent A68 iceberg will have already taken place in this region, and this response is included in the ice velocity data used to initialise our model. Finally, in the model

230   we essentially force the already detaching iceberg to have contact with ice upstream, inducing an artificial 'pulling' effect on this upstream ice, which is removed when the iceberg is calved from the domain.

When comparing our result with observations, we found that the modelled response was smaller than the internal variability in the monthly ice velocity data available. Consequently, we were unable to validate the details in spatial pattern and amplitude of our modelled response. However, the observations do show that the mean ice velocity across the shelf before and after the

235   calving event remained unchanged, or at least smaller than the measurement errors. This demonstrates that the calving of the A68 had little or no dynamic impact on the system, supporting ours and previous work that predicted such a response, or rather lack thereof.

The second aim of this work was to understand the response in GLF to the migration of the calving front back towards the GL. Here we found that as the calving front is moved from its pre-A68 location to 25 km from the GL, there is just a 13% increase

240   in GLF. It is only when regions of the shelf within 25 km of the GL are calved that ice in the narrow embayments downstream of the main tributary glaciers is removed, and this is where the increasing response in GLF begins. Calving perturbations up to this point remove more than 50% of the total ice-shelf mass, yet only induce an increase of 13% in the GLF.

Fürst et al. (2016) measured the impact of calving on the ice flux across the new marine ice front, not the GL, and therefore arrived at a different picture of buttressing on the LCIS. In their supplementary material, the impact of the same experiments

245   on ice discharge across the GL was examined, and by that definition it was found that much more of the ice-shelf area was 'passive'. We argue that it is this second definition, the integrated impact of changes in ice-shelf geometry on stresses at the GL and consequently on GLF, that is the key measure of the buttressing capability of ice shelves. This definition is in line with the original view of buttressing as the backstresses produced by an ice shelf that are felt at the grounding line (Thomas, 1979). This is the approach used in the work of Reese et al. (2018) and Zhang et al. (2020), who focus on the GLF response to ice-shelf

250   perturbations. We find that the regions with the largest 'buttressing flux response number' (Reese et al., 2018) correspond to the regions providing the majority of the buttressing in our calving experiments.

This previous work has measured the response in GLF to small perturbations in ice-shelf geometry, but by removing the entire ice shelf and calculating the instantaneous response in GLF we are able to quantify the total amount of buttressing that

the LCIS provides. This allowed us to examine what proportion of the total buttressing capacity is provided by different regions
255 in the ice shelf. We find that over 95% of the buttressing is generated by the ice in the first 25 km downstream of the GL, and
that over 80% comes from the first 5 km of ice directly downstream of the GL. The reason for this is that the LCIS geometry is
characterised by a number of small, narrow embayments where the main tributary glaciers flow into the ice shelf. It is in these
regions that the largest resistive stresses are generated, which dominate the buttressing capability of the shelf as a whole.

4.2 Ice-shelf thinning and ungrounding

260 We also set out to examine the GLF response to ice-shelf thickness perturbations. Fig. 6a shows that the response in GLF to
thinning is approximately linear as a function of the amplitude of the thickness perturbation, as long as the amplitude is less
than about 100 m (this is further explored in Appendix B). For amplitudes larger than about 100 m, the response becomes
progressively more non-linear, something that is also very evident when the GLF response is plotted as a function of the ice-
shelf mass removed (Fig. 6c). Our explanation for this pattern of GLF response is that the thickest ice in the shelf, which is
265 only reduced to the minimum ice thickness of 1 m towards the end of the series of 'uniform' experiments, is located directly
downstream of the grounding line, where the largest tributary glaciers feed into the shelf. From our calving experiments, we
saw that this is where the majority of the total buttressing capability of the ice shelf is concentrated, and therefore the largest
changes in GLF are seen when these regions of the shelf are thinned significantly.

The maximum increase in GLF due to the thinning experiments does not equal that of the calving experiments (502% vs
270 607%), as in the thinning experiments a 1 m thick layer of ice remains across the ice shelf. No thinning is applied to grounded
ice (i.e. at the Bawden and Gipps ice rises), and there remains a small, mechanical connection between these pinning points
and the GL, reducing the maximum GLF increase. When varying the minimum ice thickness, we find that increasing it to 10 m
reduces the maximum GLF response from ice-shelf thinning to 475%, whilst reducing it further to 0.001 m, only increases the
maximum GLF response to 505% from the 502% modelled with a 1 m minimum ice thickness.

275 To put the levels of ice-shelf thinning presented in Fig. 6 into context, the maximum basal melt rates observed under the LCIS
are on the order of $2 \, \mathrm{ma}^{-1}$ (Adusumilli et al., 2018), but typical values across most of the shelf are lower than this. Assuming
the maximum basal melt rate was applied across the whole ice shelf, and that the impact of the thinning is considered in an
instantaneous sense, our results suggest around 15 years of thinning is required to produce an increase in GLF of 10%, and
over 100 years of thinning to produce a doubling of GLF.

280 The dynamic response to removing the basal contacts at the Bawden and Gipps ice rises has previously been modelled with
different methods to ours. Borstad et al. (2013) only modelled the floating ice shelf, and therefore simulated a loss of contact
at the ice rises by manually adjusting their inferred ice-viscosity parameter (the equivalent of our rate factor, A). Fürst et al.
(2016) modelled the grounded ice as well as the shelf, and chose to set their basal friction coefficient to zero at the ice rises –
removing the basal traction – rather than adjusting the ice or bed geometry. Despite these differences in approach, we found
285 that our results are very similar in both spatial pattern and amplitude to these previous studies. In the experiment in which
both ice rises were removed the change in GLF was 2.2%. This suggests that, whilst these two ice rises may exert a significant

control on the flow of the shelf upstream of the pinning points, they do not exert a strong mechanical control on the ice flux at the GL, and only contribute a small amount to the total buttressing capability of the shelf.

The experiments conducted here are highly idealised in nature. We only considered 'uniform' or 'proportional' thinning
290 perturbations to the shelf, and calving front locations were determined by a 'distance to the grounding line' metric. This resulted in some unlikely calving front positions. More realistic calving experiments, using a physically based calving law or metric, could be used to model the response to more plausible ice-shelf configurations.

This work only considered the instantaneous response to perturbations in ice-shelf thickness and extent. As changes to buttressing through changing stress fields is an inherently instantaneous process, this was appropriate to explore the buttressing
295 capability of the LCIS. However, the transient response to these perturbations, in which the acceleration would induce thinning and grounding line migration, requires further study. Of particular interest is whether the instantaneous GLF increases are the peak response to the perturbation, which then attenuates, or whether the GLF response is increased further by the transient evolution of the ice geometry.

5   Conclusions

300 In this study we have examined the instantaneous response of the LCIS and its tributaries to both observed and idealised perturbations to the ice-shelf geometry. We found that the calving of the A68 iceberg in July 2017 produced a limited change (mostly < 10%) in ice velocities in the shelf and had almost no impact (a 0.5% increase) on the GLF. This finding is supported by observations which show no evidence of a change in velocity due to the calving event, and this furthermore confirms earlier work that suggested that the region that calved was largely 'passive ice'.

305 Through further, idealised calving experiments we found that a significant retreat of the calving front to 25 km downstream of the GL (removing over 50% of the ice-shelf mass) only produced a 13% increase in GLF. Further retreat of the calving front to 5 km from the GL was needed to produce a doubling of GLF. By calculating the total buttressing provided by the LCIS – through modelling the increase in GLF due to a complete collapse (607%) – we deduced that over 95% of the buttressing capability of the LCIS is provided by ice within 25 km of the GL, in the narrow embayments downstream of the main tributary
310 glaciers. We further found that over 80% of the buttressing is generated in first 5 km of ice downstream of the GL.

We also studied perturbations of increasing size to the thickness of the ice shelf. Here, again, we found that large changes to the geometry of the ice shelf are required to produce significant changes in GLF, with 30 m of thinning across the shelf inducing a 10% increase in GLF and over 200 m of thinning required to produce a doubling of GLF. Finally, we examined the response in ice velocities to the ungrounding of the ice shelf from the Bawden and Gipps ice rises, and found that whilst there
315 are significant local speedups of around 50%, there was a limited instantaneous increase in GLF of 2.2%. This suggests that whilst these pinning points control the local ice-shelf dynamics, they only provide a small amount of the total buttressing of the LCIS.
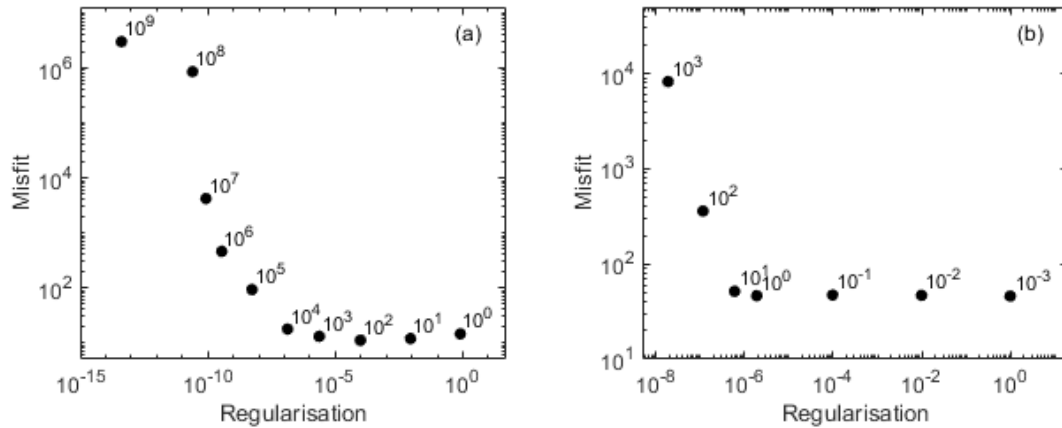
Figure A1. L-curves used to determine the amount of regularisation to apply in the optimisation of the A and C fields. **(a)** is the misfit term (I in Eq. 6) plotted as a function of the regularisation applied (R (from Eq. 7) divided by $\gamma_s^2 \times \gamma_a^2$), whilst varying γ_s (value indicated by label) with $\gamma_a = 1$. **(b)** is the misfit term plotted as a function of $R/(\gamma_s^2\gamma_a^2)$ whilst varying γ_a (value indicated by label) with $\gamma_s = 1000$.

Appendix A: L-curve analysis and A and C fields

As discussed in Sect. 2.3, an L-curve analysis was used to determine the γ_a and γ_s parameters in Eq. 7. The value of γ_s was var-
320 ied over 9 orders of magnitude and the optimisation procedure was carried out for each value of γ_s whilst γ_a was held constant. This method was then repeated varying γ_a whilst γ_s was held constant. The model-observation misfit for different amounts of regularisation is shown in Fig. A1 a and b. The chosen values were $\gamma_a = 1$ and $\gamma_s = 1000$. This amount of regularisation was then used to determine the A and C fields used throughout the experiments detailed in the main text.

The fields for the rate factor, A, and basal slipperiness parameter, C are shown in Fig. A2 a and b respectively. Examining
325 the rate factor field, we can see that softer, more deformable ice is found in the shear margins of the ice shelf and between flow units emanating from the tributary glaciers. Higher values are also seen in regions where rifts are located (e.g. upstream of the Gipps ice rise, and at the location of the rift that eventually formed the A68 iceberg).

Appendix B: Linearity of the GLF response to thinning

Fig. B1 focuses on the GLF response to smaller 'uniform' ice-shelf thickness perturbations. Over the first ~ 100 m of applied
330 thinning, the response in GLF is approximately linear, with a 0.36% increase in GLF for every 1 m of ice-shelf thickness removed. For the 'proportional' perturbations (Fig. B2) there is also an initial linear regime which extends to a 10% thinning of the shelf. In this regime there is a 1.4% increase in GLF for every 1% reduction in ice-shelf thickness.

For the 'uniform' perturbations, initially the deviation from an exact linear response is below the straight line plotted through the origin and the 0.1 m thinning point. This suggests that increasing thickness perturbations produce a relatively smaller
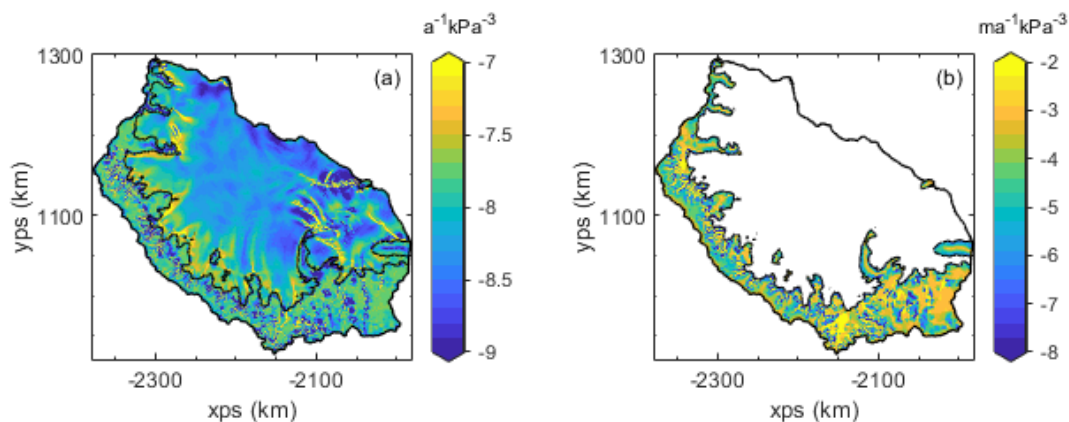
Figure A2. Maps of **(a)** the rate factor, A, in Glen's flow law (Eq. 3) and **(b)** the basal slipperiness, C, in the Weertman sliding law (Eq. 5) after optimisation as set out in Sect. 2.3. The colour bars have been saturated to allow the spatial detail in both parameters to be clearly seen.

335 increase in GLF when uniform thinning is applied. However, Fig B2 shows that when the shelf is thinned in proportion to the total ice-shelf thickness at each node, this behaviour is suppressed, and the relative response in GLF steadily increases as the proportion of the ice-shelf thickness removed increases.

The way in which the GLF response to thinning deviates below the initial linear regime is an interesting phenomena that has yet to be explained, but has been observed in previous studies on other ice shelves (e.g. Fig. S2 in Reese at al., 2018). It

340 suggests that when a uniform perturbation to ice-shelf thickness is applied across a shelf, over a certain range of perturbation size (here $\sim 1-50$ m), the relative increase in GLF is progressively reduced. From the lack of evidence of this behaviour in the proportional thinning experiments, we can see that is related to the distribution of the thickness perturbation across the shelf, and the cause of this is still unknown.

Appendix C: Mesh resolution dependence

345 To test the dependence of our results on mesh resolution, we repeated all of the experiments outlined in Sect. 2 with four additional computational meshes. In each case, the resolution around the GL was held constant at 250 m. This was to ensure that the calving and thinning experiments conducted with each mesh had the same physical extent – as a coarser resolution at the GL would mean that the calving experiments would not penetrate as close to the GL, and ice-shelf thinning would also not be applied as close to the GL.

350 The four additional meshes multiplied the original mesh resolution factors (as outlined in Sect. 2 based on ice velocities, strain rates and whether or not the element was afloat) by 0.5, 2, 3 and 4 respectively. The results of 10 experiments (5 calving and 5 uniform thinning) with the 5 different meshes are shown in Fig. C1. From this we can see that the response in GLF is
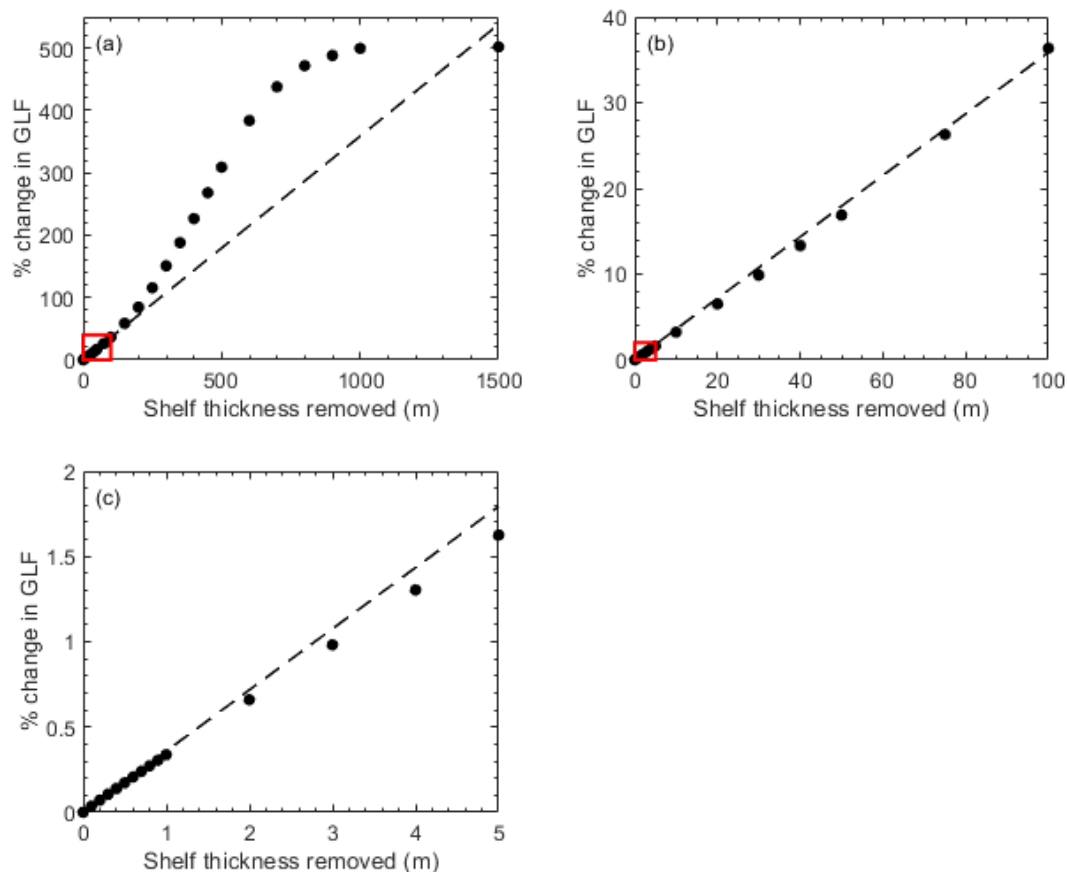
Figure B1. The percentage change in grounding line flux is plotted as a function of the 'uniform' thickness perturbation applied **(a)**. The dashed line is the straight line that passes through the origin and the 0.1 m 'uniform' thinning point. **(b)** is the region shown in the red box in panel (a), and **(c)** is the region in the red box in (b).

consistent across the 5 different mesh resolutions for each experiment, and therefore any mesh dependence of our results is negligible.
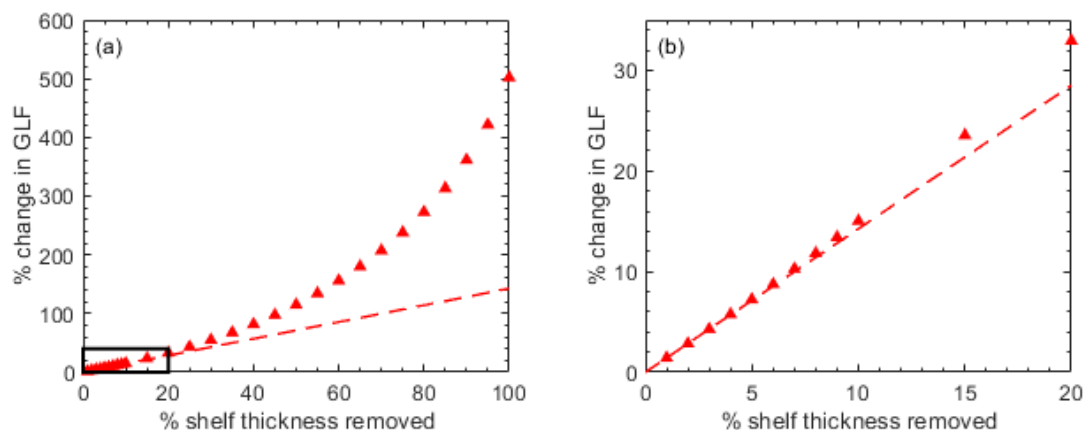
Figure B2. The percentage change in grounding line flux is plotted as a function of the 'proportional' thickness perturbation applied **(a)**. The dashed line is the straight line that passes through the origin and the 1% 'proportional' thinning point. **(b)** is the region shown in the black box in panel (a).
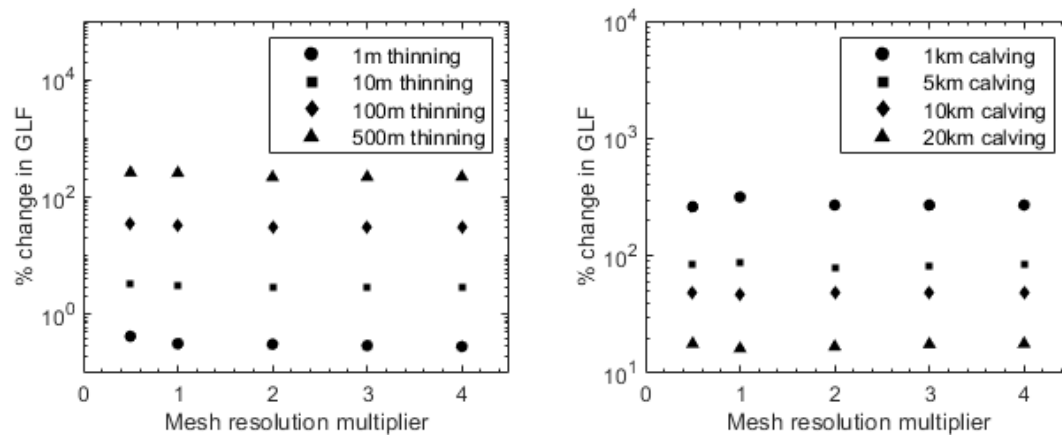
Figure C1. Mesh convergence analysis: Here, the percentage change in grounding line flux for five of the uniform thinning experiments **(a)** and five of the idealised calving experiments **(b)** are plotted for meshes in which the element sizes wer half, double, triple and quadruple the size of the original mesh used for analysis in the main text.

355 *Code and data availability.* The ice velocity dataset "ENVEO, Antarctic Ice Sheet monthly velocity maps from Copernicus Sentinel-1, 2014-2019, ESA Antarctic Ice Sheet CCI [v1.1]" is available on request from https://cryoportal.enveo.at. The source code for Úa is available at https://doi.org/10.5281/zenodo.3706624 (Gudmundsson, 2020). The model configuration scripts, raw model output and analysis scripts are available from the authors on request.

Author contributions. All authors were involved in conceiving the study. TM conducted the modelling experiments, carried out the analysis
360 and wrote the manuscript. GHG and JLB discussed the analysis and provided comments on the manuscript.

Competing interests. The authors declare that they have no conflict of interest.

Acknowledgements. TM is supported by a GW4+ Doctoral Training Partnership studentship from the Natural Environment Research Council [NE/L002434/1]. We thank Jan Wuite at ENVEO for providing the monthly observations of Antarctic ice velocity.

References

365   Adusumilli, S., Fricker, H. A., Siegfried, M. R., Padman, L., Paolo, F. S., and Ligtenberg, S. R. M.: Variable Basal Melt Rates of Antarctic Peninsula Ice Shelves, 1994-2016, Geophysical Research Letters, 45, 4086–4095, https://doi.org/10.1002/2017GL076652, 2018.

Banwell, A. F., MacAyeal, D. R., and Sergienko, O. V.: Breakup of the Larsen B Ice Shelf triggered by chain reaction drainage of supraglacial lakes, Geophysical Research Letters, 40, 5872–5876, https://doi.org/10.1002/2013GL057694, 2013.

Berthier, E., Scambos, T. A., and Shuman, C. A.: Mass loss of Larsen B tributary glaciers (Antarctic Peninsula) unabated since 2002,
370   Geophysical Research Letters, 39, 1–6, https://doi.org/10.1029/2012GL051755, 2012.

Bevan, S. L., Luckman, A. J., Hendon, H., and Wang, G.: The 2020 Larsen C Ice Shelf surface melt is a 40-year record high, The Cryosphere, 14, 3551–3564, https://doi.org/10.5194/tc-14-3551-2020, 2020.

Bindschadler, R. A., Choi, H., Wichlacz, A., Bingham, R. G., Bohlander, J. A., Brunt, K. M., Corr, H. F. J., Drews, R., Fricker, H. A., Hall, M., Hindmarsh, R. C. A., Kohler, J., Padman, L., Rack, W., Rotschky, G., Urbini, S., Vornberger, P., and Young, N. W.: Getting
375   around Antarctica: New high-resolution mappings of the grounded and freely-floating boundaries of the Antarctic ice sheet created for the International Polar Year, The Cryosphere, 5, 569–588, https://doi.org/10.5194/tc-5-569-2011, 2011.

Borstad, C. P., Rignot, E., Mouginot, J., and Schodlok, M. P.: Creep deformation and buttressing capacity of damaged ice shelves: Theory and application to Larsen C ice shelf, The Cryosphere, 7, 1931–1947, https://doi.org/10.5194/tc-7-1931-2013, 2013.

Borstad, C. P., McGrath, D., and Pope, A.: Fracture propagation and stability of ice shelves governed by ice shelf heterogeneity, Geophysical
380   Research Letters, 44, 4186–4194, https://doi.org/10.1002/2017GL072648, 2017.

Cook, A. J. and Vaughan, D. G.: Overview of areal changes of the ice shelves on the Antarctic Peninsula over the past 50 years, The Cryosphere, 4, 77–98, https://doi.org/10.5194/tc-4-77-2010, 2010.

Cornford, S. L., Seroussi, H., Asay-Davis, X. S., Gudmundsson, G. H., Arthern, R. J., Borstad, C. P., Christmann, J., Dias dos Santos, T., Feldmann, J., Goldberg, D. N., Hoffman, M. J., Humbert, A., Kleiner, T., Leguy, G. R., Lipscomb, W. H., Merino, N., Durand, G.,
385   Morlighem, M., Pollard, D., Rückamp, M., Williams, C. R., and Yu, H.: Results of the third Marine Ice Sheet Model Intercomparison Project (MISMIP+), The Cryosphere, 14, 2283–2301, https://doi.org/10.5194/tc-14-2283-2020, 2020.

De Rydt, J., Gudmundsson, G. H., Rott, H., and Bamber, J. L.: Modeling the instantaneous response of glaciers after the collapse of the Larsen B Ice Shelf, Geophysical Research Letters, 42, 5355–5363, https://doi.org/10.1002/2015GL064355, 2015.

Depoorter, M. A., Bamber, J. L., Griggs, J. A., Lenaerts, J. T. M., Ligtenberg, S. R. M., van den Broeke, M. R., and Moholdt, G.: Calving
390   fluxes and basal melt rates of Antarctic ice shelves, Nature, 502, 89–92, https://doi.org/10.1038/nature12567, 2013.

Domack, E., Duran, D., Leventer, A., Ishman, S., Doane, S., McCallum, S., Amblas, D., Ring, J., Gilbert, R., and Prentice, M.: Stability of the Larsen B ice shelf on the Antarctic Peninsula during the Holocene epoch, Nature, 436, 681–685, https://doi.org/10.1038/nature03908, 2005.

Dupont, T. K. and Alley, R. B.: Assessment of the importance of ice-shelf buttressing to ice-sheet flow, Geophysical Research Letters, 32,
395   1–4, https://doi.org/10.1029/2004GL022024, 2005.

Fürst, J. J., Durand, G., Gillet-Chaulet, F., Tavard, L., Rankl, M., Braun, M., and Gagliardini, O.: The safety band of Antarctic ice shelves, Nature Climate Change, 6, 479–482, https://doi.org/10.1038/nclimate2912, 2016.

Geuzaine, C. and Remacle, J. F.: Gmsh: a three-dimensional finite element mesh generator with built-in pre- and post-processing facilities, International Journal for Numerical Methods in Engineering, 79, 1309–1331, https://doi.org/10.1002/nme.2579, 2009.

400 Gudmundsson, G. H.: Ice-shelf buttressing and the stability of marine ice sheets, The Cryosphere, 7, 647–655, https://doi.org/10.5194/tc-7-647-2013, 2013.

Gudmundsson, G. H.: Ua Source Code: Version v2019b, Zenodo [code], https://doi.org/10.5281/zenodo.3706623, 2020.

Gudmundsson, G. H., Krug, J., Durand, G., Favier, L., and Gagliardini, O.: The stability of grounding lines on retrograde slopes, The Cryosphere, 6, 1497–1505, https://doi.org/10.5194/tc-6-1497-2012, 2012.

405 Gudmundsson, G. H., Paolo, F. S., Adusumilli, S., and Fricker, H. A.: Instantaneous Antarctic ice sheet mass loss driven by thinning ice shelves, Geophysical Research Letters, 46, 13 903–13 909, https://doi.org/10.1029/2019GL085027, 2019.

Hill, E. A., Gudmundsson, G. H., Carr, J. R., and Stokes, C. R.: Velocity response of Petermann Glacier, northwest Greenland to past and future calving events, The Cryosphere, 12, 3907–3921, https://doi.org/10.5194/tc-12-3907-2018, 2018.

Hogg, A. E. and Gudmundsson, G. H.: Commentary: Impacts of the Larsen-C Ice Shelf calving event, Nature Climate Change, 7, 540–542,
410 https://doi.org/10.1038/nclimate3359, 2017.

Holland, P. R., Brisbourne, A. M., Corr, H. F. J., McGrath, D., Purdon, K., Paden, J., Fricker, H. A., Paolo, F. S., and Fleming, A. H.: Oceanic and atmospheric forcing of Larsen C Ice-Shelf thinning, The Cryosphere, 9, 1005–1024, https://doi.org/10.5194/tc-9-1005-2015, 2015.

Jansen, D., Luckman, A. J., Cook, A. J., Bevan, S. L., Kulessa, B., Hubbard, B., and Holland, P. R.: Brief Communication: Newly developing rift in Larsen C Ice Shelf presents significant risk to stability, The Cryosphere, 9, 1223–1227, https://doi.org/10.5194/tc-9-1223-2015,
415 2015.

Khazendar, A., Rignot, E., and Larour, E. Y.: Acceleration and spatial rheology of Larsen C Ice Shelf, Antarctic Peninsula, Geophysical Research Letters, 38, 1–5, https://doi.org/10.1029/2011GL046775, 2011.

Kulessa, B., Jansen, D., Luckman, A. J., King, E. C., and Sammonds, P. R.: Marine ice regulates the future stability of a large Antarctic ice shelf, Nature Communications, 5, 1–7, https://doi.org/10.1038/ncomms4707, 2014.

420 Ligtenberg, S. R. M., Helsen, M. M., and van den Broeke, M. R.: An improved semi-empirical model for the densification of Antarctic firn, The Cryosphere, 5, 809–819, https://doi.org/10.5194/tc-5-809-2011, 2011.

MacAyeal, D. R.: Large-Scale Ice Flow Over a Viscous Basal Sediment: Theory and Application to Ice Stream B, Antarctica, Journal of Geophysical Research, 94, 4071–4087, https://doi.org/10.1029/JB094iB04p04071, 1989.

MacAyeal, D. R.: A tutorial on the use of control methods in ice-sheet modelling, Journal of Glaciology, 39, 91–98,
425 https://doi.org/10.3189/S0022143000015744, 1993.

Minchew, B. M., Simons, M., Riel, B., and Milillo, P.: Tidally induced variations in vertical and horizontal motion on Rutford Ice Stream, West Antarctica, inferred from remotely sensed observations, Journal of Geophysical Research: Earth Surface, 122, 167–190, https://doi.org/10.1002/2016JF003971, 2017.

Morlighem, M., Rignot, E., Binder, T., Blankenship, D. D., Drews, R., Eagles, G., Eisen, O., Ferraccioli, F., Forsberg, R., Fretwell, P. T.,
430 Goel, V., Greenbaum, J. S., Gudmundsson, G. H., Guo, J., Helm, V., Hofstede, C., Howat, I. M., Humbert, A., Jokat, W., Karlsson, N. B., Lee, W. S., Matsuoka, K., Millan, R., Mouginot, J., Paden, J., Pattyn, F., Roberts, J., Rosier, S., Ruppel, A., Seroussi, H., Smith, E. C., Steinhage, D., Sun, B., Broeke, M. R. v. d., Ommen, T. D. v., van Wessem, J. M., and Young, D. A.: Deep glacial troughs and stabilizing ridges unveiled beneath the margins of the Antarctic ice sheet, Nature Geoscience, 13, 132–137, https://doi.org/10.1038/s41561-019-0510-8, 2019.

435 Morris, E. M. and Vaughan, D. G.: Spatial and temporal variation of surface temperature on the Antarctic Peninsula and the limit of viability of ice shelves, Antarctic Research Series, 79, 61–68, https://doi.org/10.1029/AR079p0061, 2003.

Mouginot, J., Scheuchl, B., and Rignot, E.: Mapping of ice motion in antarctica using synthetic-aperture radar data, Remote Sensing, 4, 2753–2767, https://doi.org/10.3390/rs4092753, 2012.

Pattyn, F., Perichon, L., Durand, G., Favier, L., Gagliardini, O., Hindmarsh, R. C. A., Zwinger, T., Albrecht, T., Cornford, S. L., Docquier, D.,
440   Fürst, J. J., Goldberg, D. N., Gudmundsson, G. H., Humbert, A., Hütten, M., Huybrechts, P., Jouvet, G., Kleiner, T., Larour, E. Y., Martin, D. F., Morlighem, M., Payne, A. J., Pollard, D., Rückamp, M., Rybak, O., Seroussi, H., Thoma, M., and Wilkens, N.: Grounding-line migration in plan-view marine ice-sheet models: Results of the ice2sea MISMIP3d intercomparison, Journal of Glaciology, 59, 410–422, https://doi.org/10.3189/2013JoG12J129, 2013.

Reese, R., Gudmundsson, G. H., Levermann, A., and Winkelmann, R.: The far reach of ice-shelf thinning in Antarctica, Nature Climate
445   Change, 8, 53–57, https://doi.org/10.1038/s41558-017-0020-x, 2018.

Rignot, E., Casassa, G., Gogineni, P., Krabill, W. B., Rivera, A., and Thomas, R.: Accelerated ice discharge from the Antarctic Peninsula following the collapse of Larsen B ice shelf, Geophysical Research Letters, 31, 2–5, https://doi.org/10.1029/2004GL020697, 2004.

Rignot, E., Mouginot, J., and Scheuchl, B.: Ice flow of the Antarctic ice sheet, Science, 333, 1427–1430, https://doi.org/10.1126/science.1208336, 2011.

450 Rott, H., Skvarca, P., and Nagler, T.: Rapid Collapse of Northern Larsen Ice Shelf, Antarctica, Science, 271, 788–792, https://doi.org/10.1126/science.271.5250.788, 1996.

Rott, H., Abdel Jaber, W., Wuite, J., Scheiblauer, S., Floricioiu, D., van Wessem, J. M., Nagler, T., Miranda, N., and van den Broeke, M. R.: Changing pattern of ice flow and mass balance for glaciers discharging into the Larsen A and B embayments, Antarctic Peninsula, 2011 to 2016, The Cryosphere, 12, 1273–1291, https://doi.org/10.5194/tc-12-1273-2018, 2018.

455 Royston, S. and Gudmundsson, G. H.: Changes in ice-shelf buttressing following the collapse of Larsen A Ice Shelf, Antarctica, and the resulting impact on tributaries, Journal of Glaciology, 62, 905–911, https://doi.org/10.1017/jog.2016.77, 2016.

Scambos, T. A., Bohlander, J. A., Shuman, C. A., and Skvarca, P.: Glacier acceleration and thinning after ice shelf collapse in the Larsen B embayment, Antarctica, Geophysical Research Letters, 31, 2001–2004, https://doi.org/10.1029/2004GL020670, 2004.

Scambos, T. A., Haran, T. M., Fahnestock, M. A., Painter, T. H., and Bohlander, J. A.: MODIS-based Mosaic of Antarctica
460   (MOA) data sets: Continent-wide surface morphology and snow grain size, Remote Sensing of Environment, 111, 242–257, https://doi.org/10.1016/j.rse.2006.12.020, 2007.

Thomas, R. H.: The dynamics of marine ice sheets, Journal of Geophysical Research: Solid Earth, 24, 167–178, https://doi.org/10.3189/S0022143000014726, 1979.

van Wessem, J. M., van de Berg, W. J., Noel, B., van Meijgaard, E., Birnbaum, G., Jakobs, C. L., Krüger, K., Lenaerts, J. T. M., Lhermitte, S.,
465   Ligtenberg, S. R. M., Medley, B., Reijmer, C. H., van Tricht, K., Trusel, L. D., van Ulft, L. H., Wouters, B., Wuite, J., and van den Broeke, M. R.: Modelling the climate and surface mass balance of polar ice sheets using RACMO2, part 2: Antarctica (1979–2016), The Cryosphere, 12, 1479–1498, https://doi.org/10.5194/tc-12-1479-2018, 2018.

Vaughan, D. G., Marshall, G. J., Connolley, W. M., Parkinson, C., Mulvaney, R., Hodgson, D. A., King, J. C., Pudsey, C. J., and Turner, J.: Recent rapid regional climate warming on the Antarctic Peninsula, Climatic Change, 60, 243–274,
470   https://doi.org/10.1017/S0016756800021464, 2003.

Zhang, T., Price, S. F., Hoffman, M. J., Perego, M., and Asay-Davis, X. S.: Diagnosing the sensitivity of grounding-line flux to changes in sub-ice-shelf melting, The Cryosphere, 14, 3407–3424, https://doi.org/10.5194/tc-14-3407-2020, 2020.